universe

IMPACT FACTOR 2.6

CITESCORE 5.2

Article

Late-Time Constraints on Future Singularity Dark Energy Models from Geometry and Growth

Tomasz Denkiewicz

MDPI

https://doi.org/10.3390/universe12010014

universe

MDPI

Article

Late-Time Constraints on Future Singularity Dark Energy Models from Geometry and Growth

Tomasz Denkiewicz

Institute of Physics, University of Szczecin, Wielkopolska 15, 70-451 Szczecin, Poland;
tomasz.denkiewicz@usz.edu.pl

Abstract

We confront two future-singularity dark-energy templates—sudden future singularities (SFSs) and finite scale factor singularities (FSFSs)—with late-time geometric probes and redshift-space distortion growth data. We compute the observable growth $f\sigma_8(z)$ by solving the full linear perturbation system (including the standard fiducial cosmology rescaling of RSD measurements) and build a joint χ^2 from Pantheon+SH0ES SNe Ia, $H(z)$, DESI AP-only BAO, and $f\sigma_8$. Parameter constraints are obtained via grid-based profiling over nuisance parameters and the singularity time location parameter. We compare the viability and goodness of fit of the singularity scenarios to the ΛCDM reference.

Keywords: large-scale structure; growth of perturbations; dark energy; dynamical dark energy; cosmological singularities; DESI; Euclid; WFIRST

1. Introduction

Late-time cosmology is currently constrained primarily by *geometrical* probes, which map the background expansion through integrated distance–redshift relations. These include Type Ia supernovae, baryon acoustic oscillations, and direct measurements of $H(z)$ from cosmic chronometers and related techniques [1–12]. While these data tightly constrain the expansion history, they are intrinsically limited in their ability to identify the physical origin of cosmic acceleration: within general relativity, many distinct dark-energy histories can reproduce nearly identical background distances.

A complementary and more discriminating handle is provided by *dynamical* information, i.e., the growth of cosmic structure, commonly encoded in the observable $f\sigma_8(z)$ inferred from redshift-space distortions (RSD) in galaxy surveys [13–17]. Even though current growth data are typically less constraining than geometric probes when taken alone, their combination can substantially tighten constraints on non-standard scenarios and can test whether a given background model yields an acceptable perturbation history. This is particularly relevant for models that mimic ΛCDM at the background level but predict a modified growth rate, including both dynamical dark energy and modifications of gravity [18–21].

Among phenomenological late-time departures from ΛCDM within general relativity, an interesting class is provided by effective dark-energy models whose evolution can be associated with finite-time future singularities. These include the Sudden Future Singularity (SFS, Type II) and the Finite Scale Factor Singularity (FSFS, FSF, Type III) scenarios [22–24]. In this work we treat such models as late-time effective descriptions and assess them empirically: we do not assume that a singularity must be realized in nature, but instead ask whether the corresponding background-plus-perturbation evolution can simultaneously fit current late-time data.

Check for updates

Academic Editor: Csaba Balazs

Received: 18 November 2025
Revised: 30 December 2025
Accepted: 31 December 2025
Published: 3 January 2026

Copyright: © 2026 by the author. Licensee MDPI, Basel, Switzerland. This article is an open access article distributed under the terms and conditions of the Creative Commons Attribution (CC BY) license.

https://doi.org/10.3390/universe12010014

Motivated by this goal, we perform a joint, late-Universe comparison of SFS and FSFS models against a reference ΛCDM cosmology using a unified likelihood that combines geometric and growth information. On the geometric side we employ Type Ia supernovae, $H(z)$ measurements, and an Alcock–Paczyński-type BAO observable $F_{\rm AP}(z) = D_M(z)H(z)/c$ (here implemented using recent DESI measurements). DESI BAO-only constraints are compatible with a flat ΛCDM expansion history. At the same time, DESI analyses in the $w_0 w_a$CDM extension and in combination with CMB and/or supernova data report a statistically significant preference for evolving dark energy, whose exact significance depends on the adopted data combination [25]. On the growth side we use a compilation of $f\sigma_8(z)$ data from RSD and account for the standard geometrical rescaling associated with the fiducial cosmology adopted in each measurement [13,14,26]. To ensure numerical robustness in the presence of non-physical regions of parameter space (e.g., backgrounds leading to integration failure), we adopt a grid-based exploration with profile-likelihood minimization over nuisance parameters. In particular, we profile analytically over the supernova magnitude offset and over the clustering amplitude σ_8, optionally including a Gaussian prior on σ_8.

The paper is organized as follows: In Section 3 we define the SFS and FSFS background parameterization and summarize the mapping to the late-time observables $H(z)$ and $D_A(z)$. In Section 2 we present the linear perturbation system used to compute the scale-dependent growth and the prediction for $f\sigma_8(z)$ at a fixed wavenumber. In Section 4 we describe the data sets and the construction of the total (profiled) χ^2, including the fiducial cosmology rescaling of RSD points and the treatment of covariances. Our results—best-fit regions, goodness of fit, and a comparison to ΛCDM—are presented in Section 5. We conclude in Section 6 with a discussion of the implications and limitations of this late-time analysis.

2. Linear Perturbations and Growth of Structure

The growth of matter perturbations provides a dynamical probe complementary to purely geometrical observables. In general relativity, the exact linear perturbation equations predict a scale dependence of the growth rate on sufficiently large scales, even for ΛCDM, once the sub-Hubble approximation is relaxed [27–29].

This effect becomes particularly relevant for dynamical dark energy models, including future singularity scenarios, where dark energy perturbations may not be negligible and can couple nontrivially to matter perturbations at late times [30]. In this work we therefore solve the full set of linear perturbation equations without invoking the sub-Hubble or quasi-static approximations.

We adopt the Newtonian gauge for scalar perturbations and assume negligible anisotropic stress, so that the perturbed line element can be written as

$$ds^2 = -(1+2\Phi)\,dt^2 + (1-2\Phi)\,a^2\gamma_{ij}dx^i dx^j, \tag{1}$$

where γ_{ij} denotes the spatial metric and Φ is the Newtonian potential. For a spatially flat universe filled with pressureless, nonrelativistic dark matter with density ρ_m and an exotic dark energy component with density ρ_{de}, the background dynamics are described by the Friedmann and continuity equations,

$$H^2 = \frac{8\pi G}{3}(\rho_m + \rho_{de}), \tag{2}$$

$$\dot{\rho} = -3H(\rho + p), \tag{3}$$

where $\rho = \rho_m + \rho_{de}$ and p is the total pressure.

Linearizing Einstein's equations around this background in the Newtonian gauge yields, after some algebra, the following evolution equations for the potential Φ, the matter density contrast $\delta \equiv \delta\rho_m/\rho_m$, and the velocity potential of dark matter (encoded in $v_f \equiv -va$):

$$\begin{aligned} \ddot{\Phi} &= -4H\dot{\Phi} + 8\pi G\rho_{de}\, w_{de}\, \Phi, & (4)\\ \dot{\delta} &= 3\dot{\Phi} + \frac{k^2}{a^2} v_f, & (5)\\ \dot{v}_f &= -\Phi, & (6) \end{aligned}$$

subject to the constraint equations

$$\begin{aligned} 3H(H\Phi + \dot{\Phi}) + \frac{k^2}{a^2}\Phi &= -4\pi G\, \delta\rho_m, & (7)\\ (H\Phi + \dot{\Phi}) &= -4\pi G\, \rho_m\, v_f. & (8) \end{aligned}$$

Here, k denotes the comoving wavenumber of the perturbation mode.

If one assumes that the relevant modes are well inside the Hubble radius, $k^2/a^2 \gg H^2$, and that the gravitational potential varies slowly in time, the system above reduces to the familiar scale-independent evolution equation

$$\ddot{\delta}_m + 2H\dot{\delta}_m - 4\pi G\rho_m\delta_m = 0, \tag{9}$$

for δ_m. Relaxing only the sub-Hubble assumption, while still keeping the potential quasi-static, leads instead to a scale-dependent growth equation [28,29],

$$\ddot{\delta}_m + 2H\dot{\delta}_m - \frac{4\pi G\rho_m\delta_m}{1+\xi(a,k)} = 0, \tag{10}$$

where the function

$$\xi(a,k) = \frac{3a^2 H(a)^2}{k^2} \tag{11}$$

encodes the departure from the sub-Hubble limit. In the present analysis we do not employ any of the above approximations. All growth predictions are obtained by numerically solving the complete system of linear perturbation Equations (4)–(6) together with the background evolution specified in Section 3. The observable $f\sigma_8(z)$ used in the likelihood analysis is constructed directly from these numerical solutions.

3. FSFS and SFS as Dynamical Dark Energy Candidates

The SFS and FSFS show up within the framework of the Einstein–Friedmann cosmology governed by the standard field equations, Equation (2), and the energy-momentum conservation law, Equation (3). We obtain the SFS and FSFS scenarios with the scale factor in the following form:

$$a(t) = a_s\left[\delta + (1-\delta)\left(\frac{t}{t_s}\right)^m - \delta\left(1-\frac{t}{t_s}\right)^n\right]. \tag{12}$$

This scale factor ansatz fully specifies the background evolution and will be used consistently throughout the data analysis described in Section 4. In this work we fix the exponent m to the matter-dominated value

$$m = \frac{2}{3}. \tag{13}$$

This choice ensures that at early times ($t \ll t_s$) the scale factor reduces to the standard Einstein–de Sitter behavior $a(t) \propto t^{2/3}$ associated with pressureless matter, i.e., the ansatz reproduces a conventional pre-acceleration expansion history. Since our goal is a late-time, phenomenological test of singularity-inspired departures from ΛCDM, and the data employed here constrain primarily the late Universe, we keep m fixed and constrain the remaining parameters that control the late-time deviation and the approach to the exotic singularity (notably n, δ, and the time location parameter y_0 introduced below/in Section 4). In general, an appropriate choice of the constants (b, t_s, a_s, m, n) is necessary [22,31–33]. For both cases, the SFS as well as the FSFS model, the evolution starts with the standard big-bang singularity at $t = 0$ ($a = 0$), and evolves to an exotic singularity for $t = t_s$, where $a = a_s \equiv a(t_s)$ is a constant [32–34]. Accelerated expansion in an SFS universe is assured with a negative b, while for an FSFS universe b has to be positive. In order to have the SFS, n has to be within the range $1 < n < 2$; while for an FSFS, n has to obey the condition $0 < n < 1$. For the SFS at $t = t_s$, $a \to a_s$, $\varrho \to \varrho_s =$ const., $p \to \infty$; while for an FSFS the energy density ρ also diverges and one has: for $t \to t_s$, $a \to a_s$, $\rho \to \infty$, and $p \to \infty$, where a_s, t_s are constants and $a_s \neq 0$. In both scenarios the non-relativistic matter scales as a^{-3}, i.e.,

$$\rho_m = \Omega_{m,0}\rho_0 \left(\frac{a_0}{a}\right)^3 , \tag{14}$$

and the evolution of the exotic (dark energy) fluid ρ_{de} can be determined by taking the difference between the total energy density ρ and the energy density of the non-relativistic matter, i.e.,

$$\rho_{de} = \rho - \rho_m \ . \tag{15}$$

In those scenarios the dark energy component is also responsible for the exotic singularity at $t \to t_s$. The dimensionless energy densities are defined in a standard way as

$$\Omega_m = \frac{\rho_m}{\rho}, \quad \Omega_{de} = \frac{\rho_{de}}{\rho} \ . \tag{16}$$

For the dimensionless exotic dark energy density we have the following expression:

$$\Omega_{de} = 1 - \Omega_{m,0} \frac{H_0^2}{H^2(t)} \left(\frac{a_0}{a(t)}\right)^3 = 1 - \Omega_m. \tag{17}$$

The barotropic index of the equation of state for the dark energy is defined as

$$w_{de} = p_{de}/\rho_{de}. \tag{18}$$

The singularity scenarios considered in this work were also tested as candidates for dynamical fine structure cosmology [35]. In that approach, the dark energy is sourced by a scalar field that couples to the electromagnetic sector of the theory; the knowledge about the effective evolution of the dark energy density and the dark energy equation of state evolution is sufficient to estimate the resulting fine structure evolution.

4. Data Sets and Likelihood Construction

We confront the SFS and FSF singularity scenarios with four classes of late-time probes: (i) the Pantheon + SH0ES Type Ia supernova compilation (distance moduli with the full STAT+SYS covariance) [36–38], (ii) observational Hubble data (OHD) $H(z)$ measurements [39–45], and (iii) DESI DR2 BAO constraints in the Alcock–Paczynski (AP) combination only [25,46,47], and (iv) redshift-space distortion (RSD) growth measurements in the form of a compilation of $f\sigma_8(z)$ points with a non-diagonal covariance matrix [13,14,16,48,49][1]. For reference we also evaluate the corresponding likelihood in ΛCDM.

Throughout, we fix $H_0 = 67.36\,\mathrm{km\,s^{-1}\,Mpc^{-1}}$ and $\Omega_{m,0} = 0.3$ and treat the parameters of the singularity ansatz (including the time location parameter y_0) as the quantities to be constrained. We also keep a fixed effective comoving wavenumber $k_{\mathrm{eff}} = 0.1$ (in the same convention as used in the perturbation equations below).

4.1. Background Evolution and Geometric Functions

Using the background evolution defined in Section 3, we construct all geometrical and dynamical observables entering the likelihood.

For numerical stability and consistency across all data sets, the functions $t(z)$ and the dimensionless comoving distance $r(z)$ are obtained by solving the coupled ODE system

$$\frac{dt}{dz} = -\frac{1}{(1+z)\,H(t(z))}, \qquad \frac{dr}{dz} = \frac{H_0}{H(t(z))}, \qquad t(0) = t_0, \quad r(0) = 0, \tag{19}$$

from which we construct

$$E(z) \equiv \frac{H(z)}{H_0}, \qquad D_A(z) = \frac{r(z)}{1+z}, \qquad D_M(z) = r(z). \tag{20}$$

4.2. Pantheon + SH0ES SNe Ia with Analytic Profiling over the Absolute Magnitude

For Pantheon + SH0ES [36–38], we compute the theoretical distance modulus vector

$$\mu_{\mathrm{th}}(z) = 5\log_{10}\left[\frac{D_L(z)}{\mathrm{Mpc}}\right] + 25, \qquad D_L(z) = \frac{c}{H_0}\,r(z)\,(1+z_{\mathrm{hel}}), \tag{21}$$

evaluated at the CMB–frame redshifts z_{cmb} (with the standard $(1+z_{\mathrm{hel}})$ factor for the luminosity distance). We use the published full covariance matrix $\mathbf{C}_{\mathrm{SN}}$ (STAT + SYS).

Rather than fitting the absolute magnitude nuisance parameter explicitly, we profile over it analytically. Writing $\mathbf{1}$ for the all-ones vector and $\boldsymbol{\Delta} = \mu_{\mathrm{obs}} - \mu_{\mathrm{th}}$, the profiled supernova chi-square is implemented as

$$\chi^2_{\mathrm{SN}} = \boldsymbol{\Delta}^T \mathbf{C}_{\mathrm{SN}}^{-1} \boldsymbol{\Delta} - \frac{\left(\boldsymbol{\Delta}^T \mathbf{C}_{\mathrm{SN}}^{-1} \mathbf{1}\right)^2}{\mathbf{1}^T \mathbf{C}_{\mathrm{SN}}^{-1} \mathbf{1}} + \ln\left[\frac{\mathbf{1}^T \mathbf{C}_{\mathrm{SN}}^{-1} \mathbf{1}}{2\pi}\right], \tag{22}$$

which is the quantity minimized in our scan.

4.3. Observational Hubble Data

For the OHD compilation we use a standard Gaussian likelihood with diagonal errors,

$$\chi^2_H = \sum_i \left[\frac{H_{\mathrm{obs}}(z_i) - H_{\mathrm{th}}(z_i)}{\sigma_{H,i}}\right]^2, \tag{23}$$

where $H_{\mathrm{th}}(z_i) = H(t(z_i))$ is computed from the ODE solution for $t(z)$.

4.4. DESI DR2 BAO: AP-Only Constraints

From DESI DR2, we employ only the AP combination [46]

$$F_{\mathrm{AP}}(z) = \frac{D_M(z)\,H(z)}{c}, \tag{24}$$

for the redshift bins where AP information is provided. We build the covariance matrix using the quoted uncertainties and correlation coefficients and evaluate

$$\chi^2_{\mathrm{BAO,AP}} = (\mathbf{F}_{\mathrm{AP,obs}} - \mathbf{F}_{\mathrm{AP,th}})^T \mathbf{C}_{\mathrm{AP}}^{-1} (\mathbf{F}_{\mathrm{AP,obs}} - \mathbf{F}_{\mathrm{AP,th}}). \tag{25}$$

https://doi.org/10.3390/universe12010014

4.5. Growth Data $f\sigma_8(z)$ with Geometric Rescaling and Profiled σ_8

We use a compilation of RSD measurements [48,49] in the form of $f\sigma_8(z)$ with a covariance matrix that includes non-diagonal blocks for selected sub-samples (WiggleZ and SDSS-IV), while the remaining points are treated as uncorrelated.

Following standard practice, each measurement is corrected for the fiducial cosmology assumed in the original analysis [47]. Denoting by $E_{\rm fid}(z)$ and $D_{A,{\rm fid}}(z)$ the dimensionless Hubble parameter and angular diameter distance in the fiducial cosmology (parameterized by $\Omega_{m,0}^{\rm fid}$ as provided with each point), the prediction entering the likelihood is rescaled as

$$[f\sigma_8(z)]_{\rm pred} \;=\; \frac{E_{\rm fid}(z)\,D_{A,{\rm fid}}(z)}{E(z)\,D_A(z)}\,[f\sigma_8(z)]_{\rm th}. \tag{26}$$

For the fiducial functions we use

$$E_{\rm fid}(z) = \sqrt{\Omega_{m,0}^{\rm fid}(1+z)^3 + \left(1-\Omega_{m,0}^{\rm fid}\right)}, \qquad D_{A,{\rm fid}}(z) = \frac{1}{1+z}\int_0^z \frac{dz'}{E_{\rm fid}(z')}. \tag{27}$$

The RSD measurements constrain the standard growth combination

$$A(z) \equiv f(z)\sigma_8(z), \tag{28}$$

where $f(z) = d\ln\delta/d\ln a$ is the logarithmic growth rate and $\sigma_8(z)$ denotes the rms amplitude of *linear* matter fluctuations smoothed with a top-hat window of radius $8\,h^{-1}$Mpc at redshift z. In linear theory $\sigma_8(z)$ scales with the growth factor, which motivates Equations (28)–(30) and the linear scaling of the theory vector with the present-day amplitude $\sigma_8 \equiv \sigma_{8,0}$. In the SFS/FSF templates we therefore treat $\sigma_{8,0}$ as a nuisance amplitude and determine it by analytic profiling in the growth sector (optionally with the adopted Planck Gaussian prior), returning the corresponding best-fit $\hat{\sigma}_8$ reported in Table 1.

Table 1. Best-fit χ^2 values for the combined (ALL), geometry-only (GEOM), and growth-only (GROW) analyses. For each data set we report the minimum χ^2, the offset $\Delta\chi^2 \equiv \chi^2_{\rm min} - \chi^2_{\rm min,\Lambda CDM}$, and the corresponding best-fit parameters in the scanned (n,δ) grid after profiling over the remaining parameters (including the inner minimization over y_0; for growth, σ_8 is profiled with the adopted prior).

Data Set	**Model**	$\chi^2_{\rm min}$	$\Delta\chi^2$	n	δ	y_0	σ_8
ALL	ΛCDM	2925.53	0.00	–	–	–	0.814213
ALL	SFS	3092.43	+166.90	1.9999	−0.330067	0.9999	0.796342
ALL	FSFS	2981.37	+55.84	0.0100	0.941000	0.677318	0.812095
GEOM	ΛCDM	2909.56	0.00	–	–	–	–
GEOM	SFS	2926.37	+16.80	1.9999	−0.313568	0.9999	–
GEOM	FSFS	2947.81	+38.25	0.0264983	0.850015	0.699058	–
GROW	ΛCDM	15.9714	0.0000	–	–	–	0.814213
GROW	SFS	134.263	+118.29	1.9999	−0.792020	0.9999	0.800279
GROW	FSFS	12.5879	-3.38	0.0429967	0.866680	0.733248	0.816469

4.5.1. Perturbations and $f\sigma_8$

The growth prediction is computed by solving a first-order system for the matter density contrast $\delta(t)$ and auxiliary variables (velocity potential and metric potential variables) on the given background. Initial conditions are imposed at $z_i = 1090$, with $\delta(z_i) = 10^{-3}$ and metric/velocity initial conditions constructed from the same Poisson-type relation used consistently across models.

From the numerical solution we compute

$$f(z) = \frac{d\ln\delta}{d\ln a}, \qquad \sigma_8(z) = \sigma_{8,\mathrm{ref}}\frac{\delta(z)}{\delta(0)}. \tag{29}$$

In practice, the code uses $\sigma_{8,\mathrm{ref}} = 0.8163$ as the reference normalization built into the definition of $\sigma_8(z)$, and constructs the theory vector at this reference amplitude,

$$[f\sigma_8(z)]_{\mathrm{th,ref}} = f(z)\,\sigma_8(z)\big|_{\sigma_{8,\mathrm{ref}}}. \tag{30}$$

For an arbitrary present-day amplitude σ_8 the prediction scales linearly,

$$[f\sigma_8(z)]_{\mathrm{th}} = \left(\frac{\sigma_8}{\sigma_{8,\mathrm{ref}}}\right)[f\sigma_8(z)]_{\mathrm{th,ref}}. \tag{31}$$

4.5.2. Analytic Profiling of σ_8 with a Planck Prior

We treat σ_8 as a nuisance parameter with a Gaussian prior centered on the Planck value [49]:

$$\pi(\sigma_8) \propto \exp\left[-\frac{(\sigma_8 - \sigma_{8,\mathrm{P}})^2}{2\,\Delta\sigma_{8,\mathrm{P}}^2}\right], \qquad \sigma_{8,\mathrm{P}} = 0.8163, \quad \Delta\sigma_{8,\mathrm{P}} = 0.006. \tag{32}$$

Since the model prediction is linear in σ_8, the combined growth chi-square

$$\chi^2_G(\sigma_8) = (\mathbf{d} - \alpha\mathbf{p})^T\mathbf{C}^{-1}(\mathbf{d} - \alpha\mathbf{p}) + \left(\frac{\sigma_8 - \sigma_{8,\mathrm{P}}}{\Delta\sigma_{8,\mathrm{P}}}\right)^2, \qquad \alpha \equiv \frac{\sigma_8}{\sigma_{8,\mathrm{ref}}}, \tag{33}$$

(where $\mathbf{p}$ is the rescaled theory vector at $\sigma_{8,\mathrm{ref}}$ and $\mathbf{d}$ is the data vector) is minimized analytically with respect to σ_8, yielding both the profiled minimum $\chi^2_{G,\mathrm{prof}}$ and the best-fit $\hat{\sigma}_8$.

4.6. Total Goodness of Fit and Profiling in y_0

The total goodness of fit for a given model point is defined as

$$\chi^2_{\mathrm{tot}} = \chi^2_{\mathrm{SN}} + \chi^2_H + \chi^2_{\mathrm{BAO,AP}} + \chi^2_{G,\mathrm{prof}}, \tag{34}$$

where the growth term is already profiled over σ_8 with the Planck prior.

For each pair (n, δ) we further profile over y_0 by minimizing $\chi^2_{\mathrm{tot}}(m, n, \delta, y_0)$ in one dimension using a multi-start strategy with box constraints $y_0 \in [0.03, 0.9999]$ and additional background viability checks (positivity of $a(y)$ and $H(y)$ on the evolution interval and non-negative effective dark energy density ρ_{DE}). In the scans reported below we keep m fixed to (e.g., $m = 2/3$) as motivated in Section 3, and perform a dense grid search in (n, δ), storing the profiled best-fit values of y_0 and $\hat{\sigma}_8$ at each grid point.

4.7. Geometry-Only and Growth-Only Fits, and Profiled Contour Regions

In addition to the combined fit, we explicitly assess how the two classes of observables—(i) purely geometrical probes and (ii) growth-of-structure measurements—constrain the singularity parameters and whether they prefer compatible regions of parameter space.

We define the two partial objective functions

$$\chi^2_{\mathrm{geom}} \equiv \chi^2_{\mathrm{SN}} + \chi^2_H + \chi^2_{\mathrm{BAO,AP}}, \qquad \chi^2_{\mathrm{grow}} \equiv \chi^2_{G,\mathrm{prof}}, \tag{35}$$

where $\chi^2_{G,\mathrm{prof}}$ denotes the growth contribution after analytic profiling over σ_8 (with the adopted Planck prior), while χ^2_{SN} is already profiled over the absolute SN magnitude nuisance parameter as described above. For each model we then perform two additional scans: a geometry-only scan minimizing $\chi^2_{\rm geom}$ and a growth-only scan minimizing $\chi^2_{\rm grow}$.

As for the total likelihood, we profile over the time location parameter y_0 separately for each data subset, i.e.,

$$\chi^2_{\rm geom,prof}(n,\delta) \equiv \min_{y_0} \chi^2_{\rm geom}(m,n,\delta,y_0), \; \chi^2_{\rm grow,prof}(n,\delta) \equiv \min_{y_0} \chi^2_{\rm grow}(m,n,\delta,y_0), \quad (36)$$

subject to the same box constraints and background-viability filters used in the combined analysis. At each (n,δ) grid point we store the corresponding profiled best-fit values $\hat{y}_0$ (and, for growth, the best-fit $\hat{\sigma}_8$ returned by the analytic minimization).

To visualize the constraints, we construct profile-likelihood contour plots in the (n,δ) plane for both SFS and FSF and for each subset (GEOM and GROW). Specifically, for $X \in (\text{geom}, \text{grow})$ we define

$$\Delta\chi^2_X(n,\delta) \equiv \chi^2_{X,\rm prof}(n,\delta) - \chi^2_{X,\rm prof,min}, \quad (37)$$

where $\chi^2_{X,\rm prof,min}$ is the minimum of the corresponding profiled surface within the scanned domain. Since (n,δ) are the two displayed parameters, we report the nominal joint confidence regions using the standard two-parameter thresholds $\Delta\chi^2 = 2.30$, 6.18, 11.83 for 1σ, 2σ, and 3σ, respectively, and mark the best-fit grid point for each subset on the contour plots. This split presentation provides a direct, model-by-model diagnostic of whether tensions originate predominantly from the background (geometrical) sector or from the perturbation (growth) sector.

Because the profiling in y_0 (and, for growth, in σ_8) is performed independently for each data subset, the locations of the geometry-only and growth-only minima need not coincide. Consequently, the minimum of the combined objective function is not generally equal to the sum of the separately profiled minima,

$$\chi^2_{\rm tot,min} \neq \chi^2_{\rm geom,min} + \chi^2_{\rm grow,min}, \quad (38)$$

with equality only if both subsets are minimized by the same parameter point.

5. Results

5.1. Overview of the Scan and Profiled Likelihood

We confront the SFS and FSF future-singularity scenarios with a joint late-time likelihood built from Pantheon + SH0ES SNe Ia [36–38], observational Hubble data (OHD) [48,49], DESI DR2 BAO constraints in the AP combination only [46,47], and a compilation of $f\sigma_8(z)$ growth measurements [13,14,16,48,49]. The background evolution is specified by the analytic scale factor ansatz introduced in Section 3 and implemented in Section 4. Throughout this work we fix $(H_0, \Omega_{m,0})$ and m, and scan the singularity parameters (n,δ) on a dense grid. For each grid point we profile over the time location parameter y_0 by minimizing the total chi-square Equation (34) subject to basic viability requirements (positivity of a and H on the evolution interval and $\rho_{\rm DE} \geq 0$ along the sampled background history—see Table 2 for an explicit list of filters). Because these viability requirements act as *hard cuts* and each likelihood evaluation involves stiff ODE solves, the resulting profiled objective $\chi^2(n,\delta)$ is generally *non-smooth* and may contain holes or disconnected viable patches (especially for the FSF/FSFS template at large δ). In such a setting, a global MCMC exploration would be inefficient (low acceptance, poor mixing, and extensive tuning would be required to robustly handle frequent solver failures and hard rejections). We therefore adopt a deterministic *profile-likelihood mapping* on a regular (n,δ) grid, with explicit profiling over y_0 (and analytic profiling over the σ_8 nuisance with a Planck prior), and we infer confidence regions from $\Delta\chi^2$ contours. The stability of the inferred regions is verified by grid-resolution tests and local refinement scans (Section 5.6 and Table 3).

Table 2. Viability filters applied in the construction of the profiled χ^2 surfaces. Grid points failing any filter are rejected (equivalently assigned $\chi^2 = \infty$) and do not contribute to the profiled maps.

Filter	Criterion	Motivation/Failure Mode
Time location prior	$0.03 \leq y_0 < 1$	Excludes singularities in the past; enforces the adopted model domain.
Background positivity	$a(t) > 0$ and $H(t) > 0$ on the integration interval	Rejects non-expanding or ill-defined backgrounds.
Dark-energy viability	$\rho_{\mathrm{DE}}(t) \geq 0$ along the sampled background	Excludes unphysical effective-energy histories in the present setup.
ODE integrability (background)	Successful background solve (no NaN/Indeterminate)	Discards points where the background ODE system fails or becomes numerically unstable.
ODE integrability (perturbations)	Successful perturbation solve (no NaN/Indeterminate)	Discards points where the linear-growth system cannot be evolved reliably.

Table 3. Validation of grid-resolution stability for the all-observables profiled best fit. We compare the baseline full-range scan (61 × 61), the higher-resolution full-range scan (81 × 81), and a local refinement (zoom) around the best-fit neighborhood.

Model	Scan	$n_{\min}$	$\delta_{\min}$	$y_{0,\min}$	$\chi^2_{\min}$
SFS	61 × 61	1.9999	−0.330067	0.9999	3092.43
SFS	81 × 81	1.9999	−0.321818	0.9999	3092.65
SFS	zoom (31 × 31)	1.9999	−0.326667	0.9999	3092.41
FSFS	61 × 61	0.01	0.941	0.677318	2981.37
FSFS	81 × 81	0.01	0.941	0.677076	2981.58
FSFS	zoom (21 × 21)	0.0135	0.9185	0.693061	2980.35

The growth contribution is evaluated from the full (scale-dependent) perturbation system (Section 2), including the fiducial cosmology rescaling of each $f\sigma_8$ measurement, and with analytic profiling over σ_8 using a Gaussian Planck prior (Section 4).

For reference, we also evaluate the same data sets in a fixed ΛCDM model (with the same $(H_0, \Omega_{m,0})$ used throughout) and use its best-fit predictions as baseline curves in the figures below.

5.2. Profile–Likelihood Constraints in the (n, δ) Plane

For each model (SFS and FSF) we construct the profiled surface

$$\chi^2_{\mathrm{prof}}(n,\delta) \equiv \min_{y_0} \chi^2_{\mathrm{tot}}(m,n,\delta,y_0), \tag{39}$$

and define $\Delta\chi^2(n,\delta) = \chi^2_{\mathrm{prof}}(n,\delta) - \chi^2_{\mathrm{prof,min}}$, where $\chi^2_{\mathrm{prof,min}}$ is the global minimum of the profiled surface within the scanned domain. Since (n,δ) are the two displayed parameters, we use the standard two-parameter thresholds $\Delta\chi^2 = \{2.30, 6.18, 11.83\}$ to indicate the nominal 1σ, 2σ, and 3σ confidence regions.

Figure 1 shows that the two singularity templates exhibit qualitatively different constraint patterns. In the SFS case the fit improves toward the upper end of the scanned n-range. Motivating, dedicated, high-resolution scans in the vicinity of the boundary (and/or a broadened prior range) to assess the stability of the minimum and the local degeneracy direction. For FSF, the preferred region is pushed toward small n.

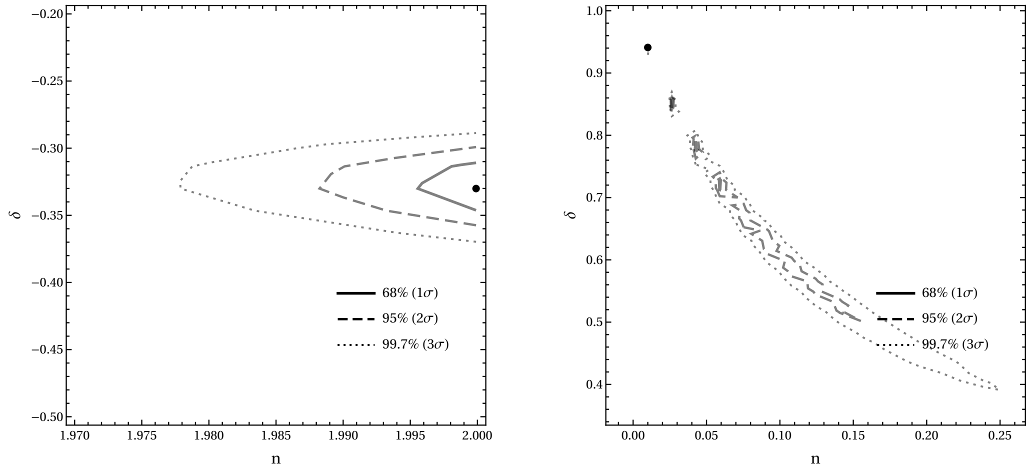

(**a**) (**b**)

Figure 1. Two-dimensional confidence contours in the (n, δ) plane for the SFS (**a**) and FSFS (**b**) models, derived from the (n, δ) grid after profiling over the remaining parameters at each grid point. Filled markers indicate the best-fit points for the corresponding data subset.

To complement the two-dimensional contours, Figure 2 presents one-dimensional profiles obtained from the same (n, δ) grid by minimizing over the remaining parameters at each grid point, including profiling in y_0. These profiles provide a compact diagnostic of whether the best fit is driven toward the edges of the scanned parameter domain.

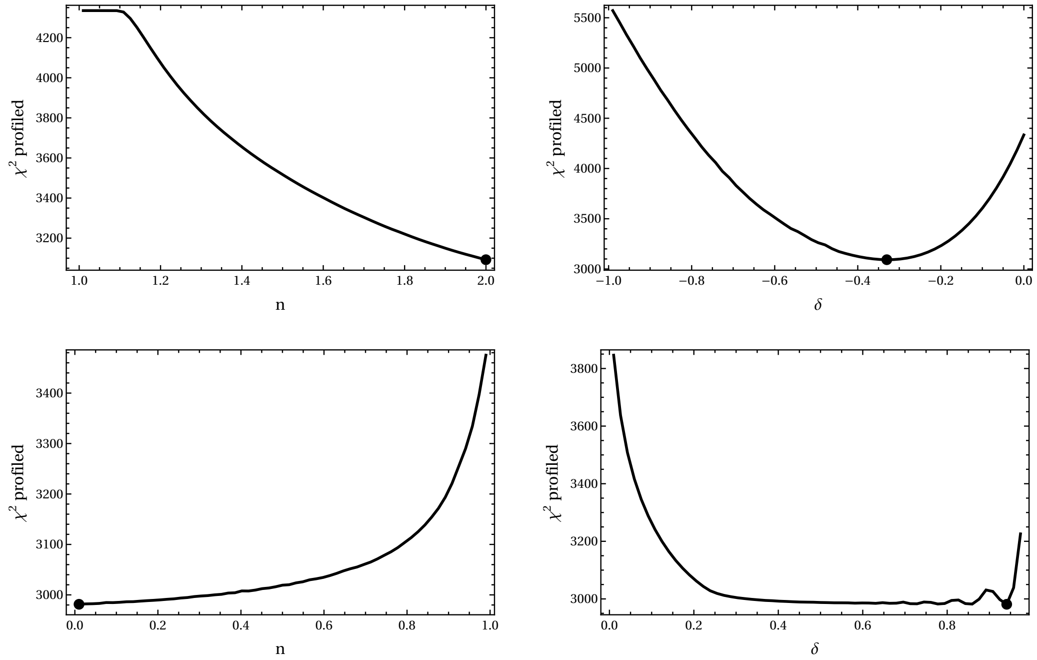

Figure 2. One -dimensional profiled χ^2 constraints derived from the (n, δ) grid by minimizing over the remaining parameters (including the inner minimization over y_0) at each grid point. (**Top row**): SFS. (**Bottom row**): FSF. Filled markers indicate the best-fit points for the corresponding data subset.

5.3. Best-Fit Predictions for Background and Growth Observables

We next compare the best-fit predictions to each data set through residual-style diagnostic plots. These figures provide an intuitive, dataset-by-dataset view of where the models succeed or fail, complementing the numerical χ^2 summary given below.

5.3.1. Growth: $f\sigma_8(z)$

Figures 3 and 4 compare the growth compilation with the best-fit SFS and FSF predictions. In each case, the theory vector is constructed using the full perturbation evolution on the best-fit background, including the fiducial cosmology rescaling and analytic profiling over σ_8 with the adopted prior, so the plotted points correspond to the quantities entering the growth likelihood.

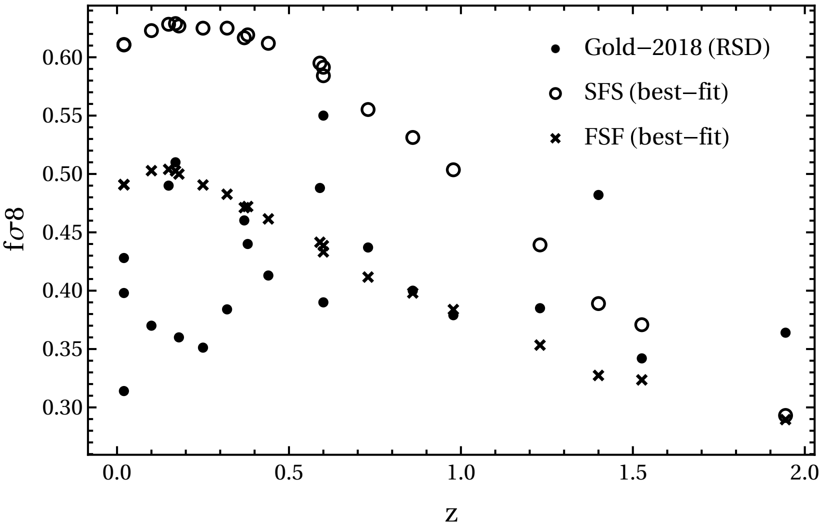

Figure 3. Comparison of the RSD growth data $f\sigma_8(z)$ with the best-fit predictions of the SFS and FSFS models. Filled circles show the observational compilation, while open circles and crosses denote the SFS and FSFS best-fit theoretical values evaluated at the same redshifts, respectively. Values are normalized by the profiled σ_8 (i.e., the amplitude is obtained by minimizing the growth-sector contribution to χ^2 with respect to σ_8 for each model).

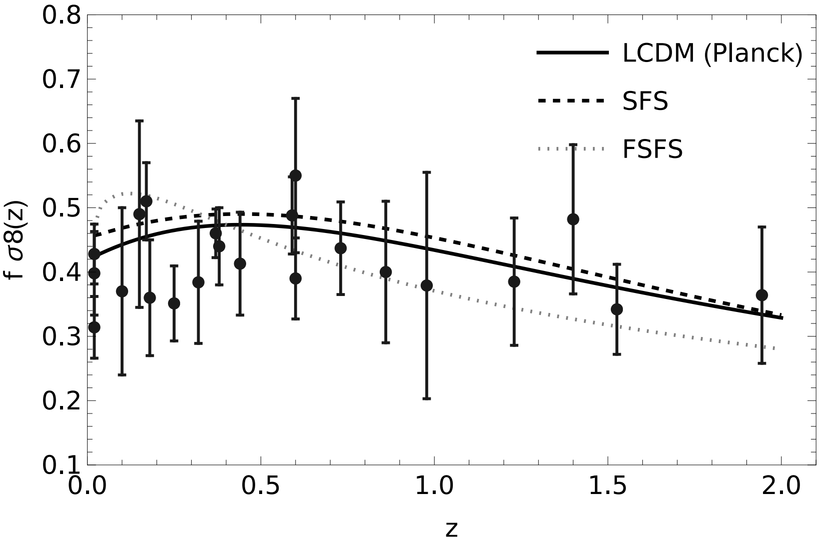

Figure 4. Redshift-space distortion measurements of $f\sigma_8(z)$ compared to the best-fit predictions of the SFS and FSFS models, as well as to the reference ΛCDM curve evaluated at the same redshifts. The SFS/FSFS theory vectors correspond to the predictions entering the growth χ^2, including the Alcock–Paczynski rescaling and profiling over σ_8.

5.3.2. Expansion Rate: $H(z)$

Figure 5 shows the observational Hubble data together with the best-fit background expansion histories of SFS and FSF, compared to the reference ΛCDM background. This plot provides a direct visual summary of the OHD contribution to the joint likelihood.

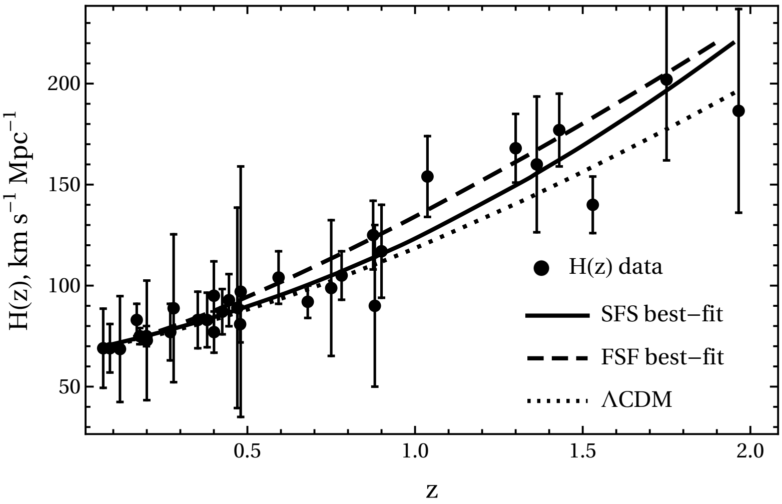

Figure 5. Observational Hubble data $H(z)$ (points with 1σ uncertainties) compared with the best-fit predictions of the SFS and FSFS models and with the reference ΛCDM cosmology.

5.3.3. BAO AP-Only: $F_{\rm AP}(z)$

Figure 6 compares the AP-only BAO constraints expressed through $F_{\rm AP}(z) = D_M(z)\, H(z)/c$ with the best-fit predictions. In this setup, $F_{\rm AP}$ acts as a geometric consistency test that complements SNe Ia and OHD.

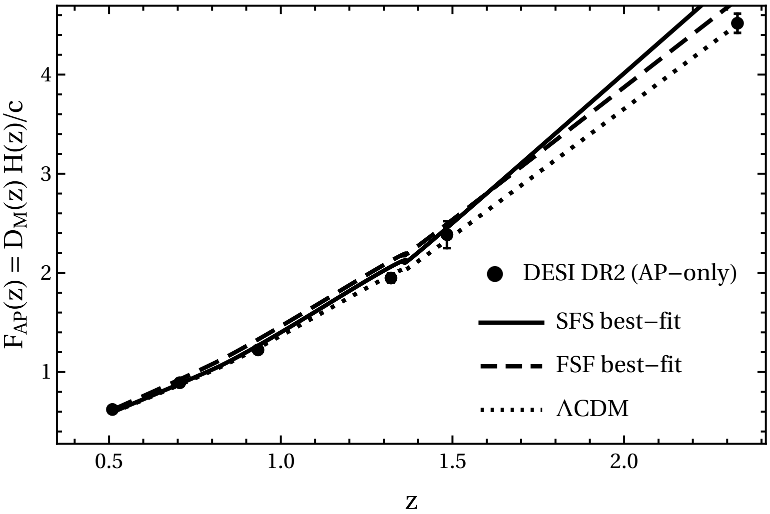

Figure 6. Alcock–Paczynski (AP) BAO constraints shown in terms of $F_{\rm AP}(z) \equiv D_M(z)\, H(z)/c$. Black points with error bars correspond to the DESI DR2 AP-only measurements, while the curves show the best-fit predictions of the SFS (solid) and FSFS (dashed) models, compared with the ΛCDM reference (dotted).

5.3.4. Supernovae: Binned Residuals with Profiled Magnitude

Figure 7 shows binned SNe Ia residuals constructed after projecting out the same absolute-magnitude mode that is profiled analytically in the SN likelihood. This representation highlights possible redshift-dependent mismatches without reintroducing sensitivity to the nuisance normalization.

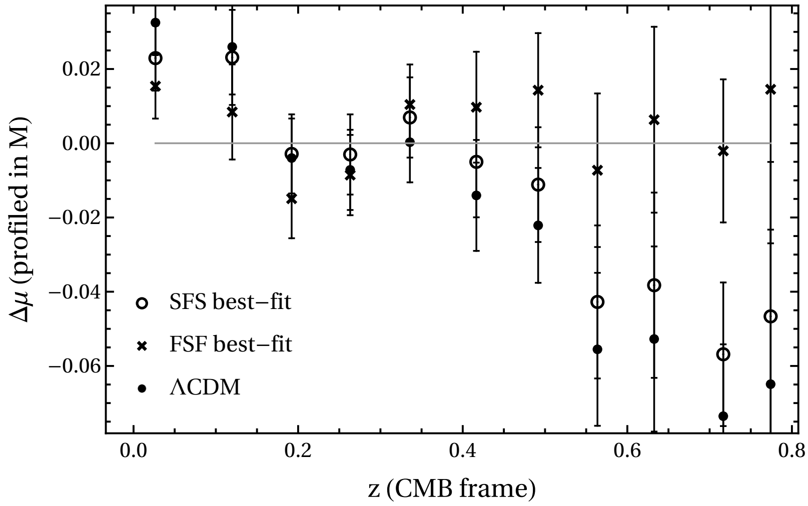

Figure 7. Binned Type Ia supernova distance-modulus residuals $\Delta\mu$ as a function of CMB-frame redshift. At each redshift, the residuals are computed after removing the same profiled mode in the absolute magnitude as used in the SN χ^2. Points represent averages in redshift bins (30 bins, requiring at least 10 SNe per bin), and error bars indicate the standard error of the mean within each bin. The best-fit SFS (open circles) and FSF (crosses) predictions are compared to the ΛCDM reference (filled dots). The horizontal line marks $\Delta\mu = 0$.

5.4. Goodness of Fit, ΛCDM Comparison, and Geometry vs. Growth Split

At the global best-fit point of each model, Equation (34), we compute the individual contributions and record, in addition, the profiled best-fit value $\hat{\sigma}_8$ returned by the analytic minimization in the growth sector. A compact summary of the best-fit parameter values and χ^2 contributions is given in Table 1.

To diagnose whether tensions arise primarily from background probes or from the perturbation sector, we also carry out separate scans for the geometry-only objective function $\chi^2_{\rm geom} = \chi^2_{\rm SN} + \chi^2_H + \chi^2_{\rm BAO,AP}$ and for the growth-only objective function $\chi^2_{\rm grow} = \chi^2_{G,\rm prof}$, profiling over y_0 independently in each case. The resulting geometry-only and growth-only constraints in the (n,δ) plane are shown in Figure 8 (SFS) and Figure 9 (FSF).

Because y_0 (and, for growth, σ_8) is profiled independently in the geometry-only and growth-only analyses, the reported minima correspond to different profiled objective functions. Consequently,

$$\chi^2_{\rm tot,min} \neq \chi^2_{\rm geom,min} + \chi^2_{\rm grow,min}, \tag{40}$$

and, more generally,

$$\min\left(\chi^2_{\rm geom} + \chi^2_{\rm grow}\right) \;\geq\; \min(\chi^2_{\rm geom}) + \min(\chi^2_{\rm grow}), \tag{41}$$

with equality only if both contributions are minimized by the same parameter point.

The split analysis highlights that the two singularity templates are constrained in markedly different ways. Within the scanned domain and under the adopted priors, SFS is primarily penalized by the growth sector, while its geometry-only fit is only moderately degraded relative to ΛCDM. Conversely, FSF can match the growth data competitively (and, in the present scan, slightly improves the growth-only minimum relative to the ΛCDM reference), but it is disfavored by geometric probes, which dominate the degradation in the combined fit.

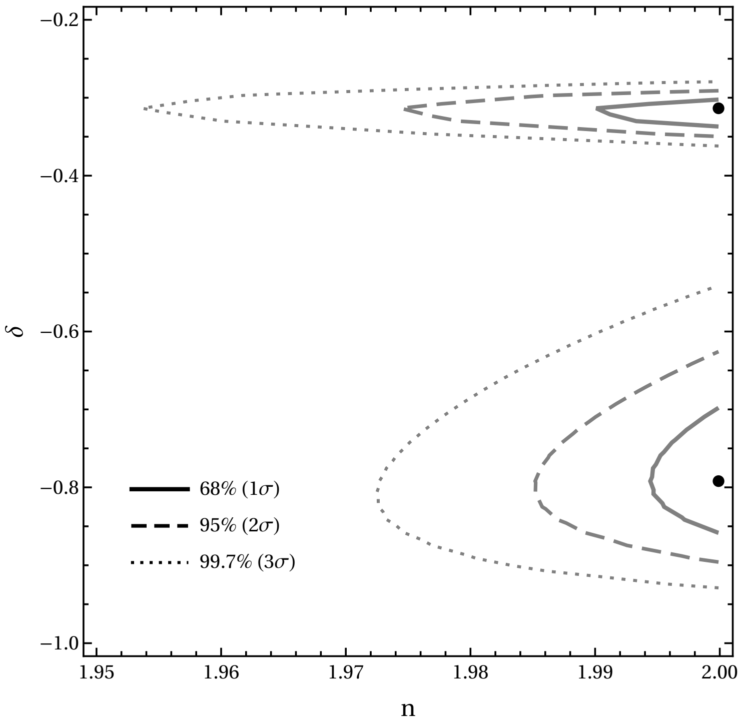

Figure 8. Two-dimensional confidence regions in the (n, δ) plane for the SFS model obtained from geometric probes (SN Ia + BAO AP-only + $H(z)$) and from growth data ($f\sigma_8$). In each case the contours correspond to $\Delta\chi^2 = \{2.30, 6.18, 11.83\}$, i.e., 68%, 95%, and 99.7% joint confidence levels for two parameters, after profiling over the remaining parameters (including y_0 and, for growth, σ_8). Filled markers indicate the best-fit points for the corresponding data subset.

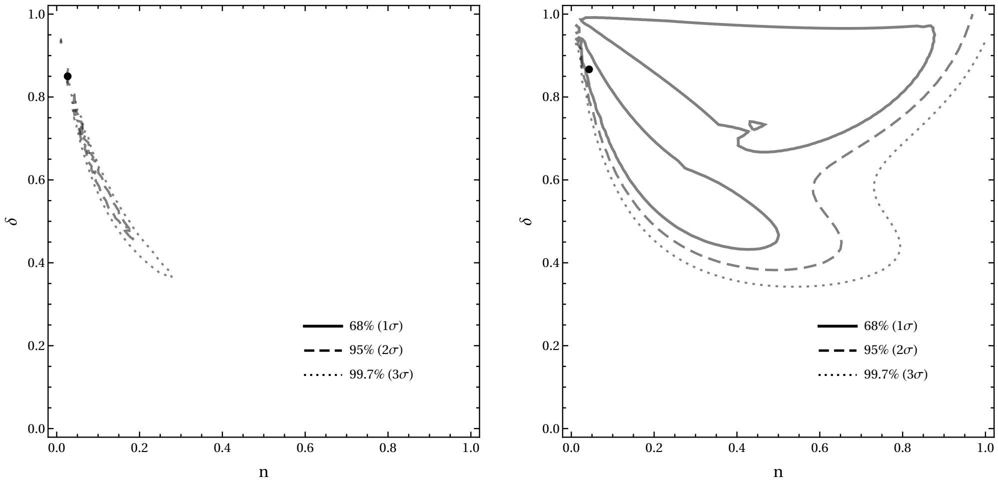

Figure 9. Two-dimensional confidence regions in the (n, δ) plane for the FSFS model obtained from the grid scan after profiling over the remaining parameters (including the inner minimization over y_0). (**Left**): geometric fit (χ^2_{geom}). (**Right**): growth fit (χ^2_{grow}). Contours correspond to the standard two-parameter $\Delta\chi^2$ thresholds. Filled markers indicate the best-fit points for the corresponding data subset.

5.5. Model-Selection Diagnostics (AIC/BIC)

In addition to the explicit χ^2 breakdown and the residual diagnostics, one may quote information criterion statistics as a compact (albeit heuristic) summary of the balance between goodness of fit and model complexity. For Gaussian errors, the Akaike and Bayesian information criteria are defined as [50,51]

$$\text{AIC} \equiv \chi^2_{\text{min}} + 2k, \qquad \text{BIC} \equiv \chi^2_{\text{min}} + k \ln N, \tag{42}$$

where k is the number of fitted (free) parameters and N is the number of data points used in the given fit.

In our setup, the number of data points entering each likelihood block is

$$N_{\rm SN} = 1701, \qquad N_H = 31, \qquad N_{\rm BAO,AP} = 6, \qquad N_{f\sigma_8} = 22, \tag{43}$$

hence $N_{\rm geom} = N_{\rm SN} + N_H + N_{\rm BAO,AP} = 1738$, $N_{\rm grow} = N_{f\sigma_8} = 22$, $N_{\rm all} = N_{\rm geom} + N_{\rm grow} = 1760$. For parameter counting, we treat the singularity parameters (n, δ) and the time location parameter y_0 as free in SFS/FSFS, and we include the growth normalization σ_8 as a nuisance parameter in the growth sector (profiled analytically with the adopted Planck prior). With $(H_0, \Omega_{m,0}, m)$ fixed throughout, this implies

$$k_{\Lambda\rm CDM} = \begin{cases} 0, & \text{GEOM}, \\ 1, & \text{GROW/ALL}, \end{cases} \qquad k_{\rm SFS} = k_{\rm FSFS} = \begin{cases} 3, & \text{GEOM}, \\ 4, & \text{GROW/ALL}, \end{cases} \tag{44}$$

so that the relative penalty with respect to ΛCDM is $\Delta k = 3$ in all three comparisons. Accordingly,

$$\Delta\text{AIC} = \Delta\chi^2 + 2\Delta k = \Delta\chi^2 + 6, \qquad \Delta\text{BIC} = \Delta\chi^2 + \Delta k \ln N = \Delta\chi^2 + 3\ln N, \tag{45}$$

with $N = N_{\rm geom}, N_{\rm grow}, N_{\rm all}$ depending on the data set.

The resulting information criterion values for all three data combinations (GEOM, GROW, and ALL) are summarized in Table 4. For each data set we list the minimum χ^2, together with $\Delta\chi^2$, ΔAIC, and ΔBIC relative to the corresponding ΛCDM baseline (computed using the same N and $\Delta k = 3$ as detailed above).

We stress that AIC/BIC are only heuristic summaries; the more informative comparison remains the explicit chi-square breakdown and the residual plots for each data set.

Table 4. Information criterion summary for the geometry-only (GEOM), growth-only (GROW), and combined (ALL) fits. We report $\chi^2_{\rm min}$ for each model, and the offsets $\Delta\chi^2$, ΔAIC, and ΔBIC computed with respect to the corresponding ΛCDM baseline for the same data set. Here $N_{\rm geom} = 1738$, $N_{\rm grow} = 22$, and $N_{\rm all} = 1760$. The parameter counts are $k_{\Lambda\rm CDM} = 0$ (GEOM) and $k_{\Lambda\rm CDM} = 1$ (GROW/ALL), while $k_{\rm SFS} = k_{\rm FSFS} = 3$ (GEOM) and $k_{\rm SFS} = k_{\rm FSFS} = 4$ (GROW/ALL), so $\Delta k = 3$ for all comparisons.

Data Set	Model	N	$\chi^2_{\rm min}$	$\Delta\chi^2$	ΔAIC	ΔBIC
ALL	ΛCDM	1760	2925.53	0.00	0.00	0.00
ALL	SFS	1760	3092.43	166.90	172.90	189.32
ALL	FSFS	1760	2981.37	55.84	61.84	78.26
GEOM	ΛCDM	1738	2909.56	0.00	0.00	0.00
GEOM	SFS	1738	2926.37	16.81	22.81	39.19
GEOM	FSFS	1738	2947.81	38.25	44.25	60.63
GROW	ΛCDM	22	15.97	0.00	0.00	0.00
GROW	SFS	22	134.26	118.29	124.29	127.56
GROW	FSFS	22	12.59	−3.38	2.62	5.89

5.6. Validation: Grid-Resolution Stability and Local Refinement

To assess the numerical stability of the profiled grid results, we performed two cross-checks for the *all-observables* likelihood: (i) a full-range scan with increased grid resolution (from 61 × 61 to 81 × 81 points in the same (n, δ) domain) and (ii) a local "zoom" refinement around the profiled best-fit neighborhood. In all cases we used identical priors and the same one-dimensional profiling over the time location parameter y_0 at each grid node. The resulting best-fit locations and minimum values are summarized in Table 3.

5.6.1. Sudden Future Singularity

The 81×81 full-range scan reproduces the same boundary-dominated best-fit behavior found in the 61×61 baseline scan, with only a minor shift along the δ direction (Table 3). A dedicated local refinement in the neighborhood of the minimum (zoom scan) yields a consistent best-fit region and a practically unchanged minimum χ^2, indicating that the inferred constraints are not sensitive to the baseline grid spacing in (n, δ).

5.6.2. Finite Scale Factor Singularity

As summarized in Table 3, increasing the global grid resolution from 61×61 to 81×81 preserves the location of the best-fit region in the profiled (n, δ) surface. A dedicated local refinement yields a slightly lower $\chi^2_{\rm min}$ and shifts the profiled minimum along the same shallow valley. This behavior is expected because, in the high-δ regime, the one-dimensional profile in y_0 becomes numerically rugged due to stiff ODE solves combined with hard viability cuts. Concretely, for the 21×21 local refinement, only 252 out of 441 grid nodes remain viable after the filters in Table 2 (the rest are rejected by non-physical background histories and/or numerical failures). Importantly, the resulting $\mathcal{O}(1)$ changes in the minimum do not modify the inferred confidence contours or any qualitative conclusions drawn from the baseline maps.

Given this level of stability under both global refinement and local zooming, we adopt the 61×61 grid as the reference for figures and summary tables in the main text, the 81×81 full-range runs and the local zoom refinements yield indistinguishable best-fit regions and only sub-percent shifts in the profiled minima; hence, the higher-resolution and zoom scans are used solely as validation checks (Table 3).

6. Conclusions

We have tested two singularity-inspired dynamical dark-energy templates, SFS and FSFS, against a combined late-time likelihood built from Pantheon + SH0ES SNe Ia [36–38], OHD $H(z)$ measurements [39–45], DESI DR2 BAO constraints in the AP combinationi [25,46,47], and a compilation of RSD growth measurements in the form of $f\sigma_8(z)$ [13,14,16,48,49]. A central feature of the analysis is that the growth predictions are obtained from the full (scale-dependent) linear perturbation system evolved on the model background, with a consistent fiducial cosmology rescaling of each RSD point and analytic profiling over σ_8 with a Planck-motivated Gaussian prior. The parameter inference is performed via dense scans in the (n, δ) plane with profiling over the singularity time location parameter y_0 at each grid point, subject to background viability filters. The results show a clear qualitative separation between the two scenarios when assessed jointly and also when split into geometry-only and growth-only constraints. For SFS, the best-fit region is driven toward the upper boundary of the explored n range, and while the geometry-only sector can be accommodated at a moderately degraded level relative to ΛCDM, the growth likelihood strongly penalizes the model within the scanned domain. In the combined analysis, this manifests as a substantial deterioration of the total goodness of fit relative to the ΛCDM reference.

For FSFS, the pattern is different: the growth sector can be fitted competitively (and, within the present scan, yields a slightly improved growth-only minimum relative to ΛCDM), but geometric probes disfavor the model and dominate the degradation of the combined fit. The geometry vs. growth contour comparison therefore indicates that, in the adopted parametrization and prior ranges, FSFS is constrained primarily through background observables, whereas SFS is constrained primarily through structure-growth data.

These conclusions should be interpreted within the deliberately restricted scope of the present analysis: $(H_0, \Omega_{m,0})$ and m are held fixed; BAO information is used only through the AP combination (without an absolute ruler calibration in this setup); and σ_8 is treated as a nuisance parameter with an external prior.

The SFS/FSFS scenarios considered here are defined via a phenomenological parametrization of the scale factor $a(t)$. Consequently, a substantial fraction of parameter combinations leads to either no viable background evolution or to configurations that fall outside the physical domain of the present formulation. In particular, the parameter y_0 controls the location of the future singularity in the adopted parametrization, and values $y_0 > 1$ would correspond to a singularity in the past and therefore to non-physical solutions within the present setup. We thus impose $y_0 < 1$ as a hard prior and discard all parameter points that fail to produce a physical background (and, when relevant, a well-defined growth solution). Within the physical domain ($y_0 < 1$) and for fixed $m = 2/3$, the SFS likelihood improves monotonically towards the boundary $y_0 \to 1^-$ and $n \to 2^-$. Accordingly, the best-fit points saturate the imposed upper bounds in both the joint and split analyses. We interpret this behavior as a limitation of the underlying scale factor parametrization: the fit is driven towards the boundary where the model most closely mimics a standard background evolution, rather than as a robust prediction of an imminent singularity. Importantly, even in this boundary regime the SFS model provides a very poor description of the $f\sigma_8$ data, which dominates the degradation of the combined fit relative to ΛCDM.

Funding: This research received no external funding.

Institutional Review Board Statement: Not applicable.

Informed Consent Statement: Not applicable.

Data Availability Statement: The raw data supporting the conclusions of this article will be made available by the author on request.

Conflicts of Interest: The author declares no conflicts of interest.

Abbreviations

The following abbreviations are used in this manuscript:

ΛCDM	Lambda Cold Dark Matter
SFS	Sudden Future Singularity
FSFS	Finite Scale Factor Singularity
DESI	Dark Energy Spectroscopic Instrument
CMB	Cosmic Microwave Background
BAO	Baryon Acoustic Oscillations
SNeIa	Type Ia Supernovae
LSS	Large-Scale Structure

Note

[1] All calculations and figures were produced using *Mathematica* (Wolfram Research, Inc., *Mathematica*, Version 13.0, Champaign, IL (2021)).

References

1. Riess, A.G.; Filippenko, A.V.; Challis, P.; Clocchiatti, A.; Diercks, A.; Garnavich, P.M.; Gillil, R.L.; Hogan, C.J.; Jha, S.; Kirshner, R.P.; et al. Observational Evidence from Supernovae for an Accelerating Universe and a Cosmological Constant. *Astron. J.* **1998**, *116*, 1009–1038. [CrossRef]

2. Perlmutter, S.; Aldering, G.; Goldhaber, G.; Knop, R.A.; Nugent, P.; Castro, P.G.; Deustua, S.; Fabbro, S.; Goobar, A.; Groom, D.E.; et al. Measurements of Ω and Λ from 42 High-Redshift Supernovae. *Astrophys. J.* **1999**, *517*, 565–586. [CrossRef]
3. Suzuki, N.; Rubin, D.; Lidman, C.; Aldering, G.; Amanullah, R.; Barbary, K.; Barrientos, L.F.; Botyanszki, J.; Brodwin, M.; Connolly, N.; et al. The Hubble Space Telescope Cluster Supernova Survey: V. Improving the Dark Energy Constraints Above z > 1 and Building an Early-Type-Hosted Supernova Sample. *Astrophys. J.* **2012**, *746*, 85. [CrossRef]
4. Betoule, M.; Marriner, J.; Regnault, N.; Cuillandre, J.C.; Astier, P.; Guy, J.; Ball, C.; El Hage, P.; Hardin, D.; Kessler, R.; et al. Improved Photometric Calibration of the SNLS and the SDSS Supernova Surveys. *Astron. Astrophys.* **2013**, *552*, A124. [CrossRef]
5. Eisenstein, D.J.; Zehavi, I.; Hogg, D.W.; Scoccimarro, R.; Blanton, M.R.; Nichol, R.C.; Scranton, R.; Seo, H.J.; Tegmark, M.; Zheng, Z.; et al. Detection of the Baryon Acoustic Peak in the Large-Scale Correlation Function of SDSS Luminous Red Galaxies. *Astrophys. J.* **2005**, *633*, 560–574. [CrossRef]
6. Bassett, B.A.; Hlozek, R. Baryon Acoustic Oscillations. *arXiv* **2009**. [CrossRef] [PubMed]
7. Alam, S.; Ata, M.; Bailey, S.; Beutler, F.; Bizyaev, D.; Blazek, J.A.; Bolton, A.S.; Brownstein, J.R.; Burden, A.; Chuang, C.H.; et al. The clustering of galaxies in the completed SDSS-III Baryon Oscillation Spectroscopic Survey: Cosmological analysis of the DR12 galaxy sample. *Mon. Not. R. Astron. Soc.* **2017**, *470*, 2617–2652. [CrossRef]
8. Alam, S.; Aubert, M.; Avila, S.; Ball, C.; Bautista, J.E.; Bershady, M.A.; Bizyaev, D.; Blanton, M.R.; Bolton, A.S.; Bovy, J.; et al. The Completed SDSS-IV extended Baryon Oscillation Spectroscopic Survey: Cosmological Implications from two Decades of Spectroscopic Surveys at the Apache Point observatory. *arXiv* **2020**. [CrossRef]
9. Aghanim, N.; Akrami1, Y.; Ashdown, M.; Aumont, J.; Baccigalupi, C.; Ballardini, M.; Banday, A.J.; Barreiro, R.B.; Bartolo, N.; Basak, S.; et al. Planck 2018 results. VI. Cosmological parameters. *Astron. Astrophys.* **2020**, *641*, A6. [CrossRef]
10. Weinberg, D.H.; Mortonson, M.J.; Eisenstein, D.J.; Hirata, C.; Riess, A.G.; Rozo, E. Observational Probes of Cosmic Acceleration. *Phys. Rept.* **2013**, *530*, 87–255. [CrossRef]
11. Salzano, V.; Rodney, S.A.; Sendra, I.; Lazkoz, R.; Riess, A.G.; Postman, M.; Broadhurst, T.; Coe, D. Improving Dark Energy Constraints with High Redshift Type Ia Supernovae from CANDELS and CLASH. *Astron. Astrophys.* **2013**, *557*, A64. [CrossRef]
12. Lazkoz, R.; Alcaniz, J.; Escamilla-Rivera, C.; Salzano, V.; Sendra, I. BAO cosmography. *J. Cosmol. Astropart. Phys.* **2013**, *1312*, 5. [CrossRef]
13. Nesseris, S.; Pantazis, G.; Perivolaropoulos, L. Tension and constraints on modified gravity parametrizations of Geff(z) from growth rate and Planck data. *Phys. Rev. D* **2017**, *96*, 023542. [CrossRef]
14. Sagredo, B.; Nesseris, S.; Sapone, D. Internal robustness of growth rate data. *Phys. Rev. D* **2018**, *98*, 083543. [CrossRef]
15. Ade, P.A.R.; Aghanim, N.; Arnaud, M.; Ashdown, M.; Aumont, J.; Baccigalupi, C.; Banday, A.J.; Barreiro, R.B.; Bartlett, J.G.; Bartolo, N.; et al. Planck 2015 results. XIII. Cosmological parameters. *arxiv* **2015**. [CrossRef]
16. Alam, S.; Ho, S.; Silvestri, A. Testing deviations from LCDM with growth rate measurements from six large-scale structure surveys at $z = 0.06$–1. *Mon. Not. R. Astron. Soc.* **2016**, *456*, 3743–3756. [CrossRef]
17. Albarran, I.; Bouhmadi-López, M.; Morais, J. Cosmological perturbations in an effective and genuinely phantom dark energy Universe. *Phys. Dark Universe* **2017**, *16*, 94–108. [CrossRef]
18. Tsujikawa, S.; Gannouji, R.; Moraes, B.; Polarski, D. The dispersion of growth of matter perturbations in f(R) gravity. *Phys. Rev.* **2009**, *D80*, 084044. [CrossRef]
19. Gannouji, R.; Moraes, B.; Polarski, D. The growth of matter perturbations in f(R) models. *J. Cosmol. Astropart. Phys.* **2009**, *2009*, 34. [CrossRef]
20. Linder, E.V.; Cahn, R.N. Parameterized Beyond-Einstein Growth. *Astropart. Phys.* **2007**, 28, 481–488. [CrossRef]
21. Bamba, K.; Lopez-Revelles, A.; Myrzakulov, R.; Odintsov, S.D.; Sebastiani, L. Cosmic history of viable exponential gravity: Equation of state oscillations and growth index from inflation to dark energy era. *Class. Quant. Grav.* **2013**, *30*, 015008. [CrossRef]
22. Barrow, J.D. Sudden future singularities. *Class. Quant. Grav.* **2004**, *21*, L79–L82. [CrossRef]
23. Barrow, J.D.; Tsagas, C.G. Structure and stability of the Lukash plane-wave spacetime. *Class. Quant. Grav.* **2005**, *22*, 825–840. [CrossRef]
24. Nojiri, S.; Odintsov, S.D. Inhomogeneous equation of state of the universe: Phantom era, future singularity and crossing the phantom barrier. *Phys. Rev.* **2005**, *D72*, 023003. [CrossRef]
25. Adame, A.; Aguilar, J.; Ahlen, S.; Alam, S.; Alexander, D.M.; Alvarez, M.; Alves, O.; Anand, A.; Andrade, U.; Armengaud, E.; et al. DESI 2024 VI: Cosmological Constraints from the Measurements of Baryon Acoustic Oscillations. *J. Cosmol. Astropart. Phys.* **2025**, *2025*, 21. [CrossRef]
26. Beutler, F.; Saito, S.; Seo, H.J.; Brinkmann, J.; Dawson, K.S.; Eisenstein, D.J.; Font-Ribera, A.; Ho, S.; McBride, C.K.; Montesano, F.; et al. The clustering of galaxies in the SDSS-III Baryon Oscillation Spectroscopic Survey: Testing gravity with redshift-space distortions using the power spectrum multipoles. *Mon. Not. R. Astron. Soc.* **2014**, *443*, 1065–1089. [CrossRef]
27. Dent, J.B.; Dutta, S. On the dangers of using the growth equation on large scales in the Newtonian gauge. *Phys. Rev. D* **2009**, *79*, 063516. [CrossRef]

28. Dent, J.B.; Dutta, S.; Perivolaropoulos, L. New Parametrization for the Scale Dependent Growth Function in General Relativity. *Phys. Rev.* **2009**, *D80*, 023514. [CrossRef]
29. Perivolaropoulos, L. Consistency of LCDM with Geometric and Dynamical Probes. *J. Phys. Conf. Ser.* **2010**, *222*, 012024. [CrossRef]
30. Denkiewicz, T. Dark energy and dark matter perturbations in singular universes. *J. Cosmol. Astropart. Phys.* **2015**, *37*, 37. [CrossRef]
31. Dąbrowski, M.P.; Denkiewicz, T.; Hendry, M.A. How far is it to a sudden future singularity of pressure? *Phys. Rev.* **2007**, *D75*, 123524. [CrossRef]
32. Nojiri, S.; Odintsov, S.D. Unified cosmic history in modified gravity: From F(R) theory to Lorentz non-invariant models. *Phys. Rep.* **2011**, *505*, 59–144. [CrossRef]
33. Cattoën, C.; Visser, M. Necessary and sufficient conditions for big bangs, bounces, crunches, rips, sudden singularities and extremality events. *Class. Quantum Gravity* **2005**, *22*, 4913–4930. [CrossRef]
34. Fernández-Jambrina, L.; Lazkoz, R. Geodesic behavior of sudden future singularities. *Phys. Rev. D* **2004**, *70*, 121503. [CrossRef]
35. Dąbrowski, M.P.; Denkiewicz, T.; Martins, C.J.A.P.; Vielzeuf, P.E. Variations of the fine-structure constant α in exotic singularity models. *Phys. Rev. D* **2014**, *89*, 123512. [CrossRef]
36. Scolnic, D.; Brout, D.; Carr, A.; Riess, A.G.; Davis, T.M.; Dwomoh, A.; Jones, D.O.; Ali, N.; Charvu, P.; Chen, R.; et al. The Pantheon + Analysis: The Full Data Set and Light-curve Release. *Astrophys. J.* **2022**, *938*, 113. [CrossRef]
37. Brout, D.; Scolnic, D.; Popovic, B.; Riess, A.G.; Carr, A.; Zuntz, J.; Kessler, R.; Davis, T.M.; Hinton, S.; Jones, D.; et al. The Pantheon + Analysis: Cosmological Constraints. *Astrophys. J.* **2022**, *938*, 110. [CrossRef]
38. Riess, A.G.; Yuan, W.; Macri, L.M.; Scolnic, D.; Brout, D.; Casertano, S.; Jones, D.O.; Murakami, Y.; Anand, G.S.; Breuval, L.; et al. A Comprehensive Measurement of the Local Value of the Hubble Constant with 1 km s^{-1} Mpc^{-1} Uncertainty from the Hubble Space Telescope and the SH0ES Team. *Astrophys. J. Lett.* **2022**, *934*, L7. [CrossRef]
39. Jimenez, R.; Verde, L.; Treu, T.; Stern, D. Constraints on the Equation of State of Dark Energy and the Hubble Constant from Stellar Ages and the Cosmic Microwave Background. *Astrophys. J.* **2003**, *593*, 622–629. [CrossRef]
40. Simon, J.; Verde, L.; Jimenez, R. Constraints on the redshift dependence of the dark energy potential. *Phys. Rev. D* **2004**, *71*, 123001. [CrossRef]
41. Stern, D.; Jimenez, D.; Verde, R.; Kamionkowski, L.; Stanford, M.; Adam, S. Cosmic Chronometers: Constraining the Equation of State of Dark Energy. I: H(z) Measurements. *J. Cosmol. Astropart. Phys.* **2010**, *2010*, 8. [CrossRef]
42. Moresco, M.; Cimatti, A.; Jimenez, R.; Pozzetti, L.; Zamorani, G.; Bolzonella, M.; Dunlop, J.; Lamareille, F.; Mignoli, M.; Pearce, H.; et al. Improved constraints on the expansion rate of the Universe up to z∼1.1 from the spectroscopic evolution of cosmic chronometers. *J. Cosmol. Astropart. Phys.* **2012**, *2012*, 6. [CrossRef]
43. Moresco, M. Raising the bar: New constraints on the Hubble parameter with cosmic chronometers at $z{\sim}2$. *Mon. Not. R. Astron. Soc. Lett.* **2015**, *450*, L16–L20. [CrossRef]
44. Moresco, M.; Pozzetti, L.; Cimatti, A.; Jimenez, R.; Maraston, C.; Verde, L.; Thomas, D.; Citro, A.; Tojeiro, R.; Wilkinson, D. A 6 of the epoch of cosmic re-acceleration. *J. Cosmol. Astropart. Phys.* **2016**, *2016*, 14. [CrossRef]
45. Borghi, N.; Moresco, M.; Cimatti, A. Toward a Better Understanding of Cosmic Chronometers: A New Measurement of H(z) at z∼0.7. *Astrophys. J. Lett.* **2021**, *928*, L4. [CrossRef]
46. Alcock, C.; Paczynski, B. An Evolution Free Test for Non-Zero Cosmological Constant. *Nature* **1979**, *281*, 358–359. [CrossRef]
47. Ballinger, W.E.; Peacock, J.A.; Heavens, A.F. Measuring the cosmological constant with redshift surveys. *Mon. Not. R. Astron. Soc.* **1996**, *282*, 877–888. [CrossRef]
48. Kaiser, N. Clustering in real space and in redshift space. *Mon. Not. R. Astron. Soc.* **1987**, *227*, 1–21. [CrossRef]
49. Hamilton, A.J.S. Linear Redshift Distortions: A Review. In *The Evolving Universe*; Astrophysics and Space Science Library; Springer: Berlin/Heidelberg, Germany, 1998; Volume 231, pp. 185–275. [CrossRef]
50. Akaike, H. A new look at the statistical model identification. *IEEE Trans. Autom. Control* **1974**, *19*, 716–723. [CrossRef]
51. Schwarz, G. Estimating the Dimension of a Model. *Ann. Stat.* **1978**, *6*, 461–464. [CrossRef]

Disclaimer/Publisher's Note: The statements, opinions and data contained in all publications are solely those of the individual author(s) and contributor(s) and not of MDPI and/or the editor(s). MDPI and/or the editor(s) disclaim responsibility for any injury to people or property resulting from any ideas, methods, instructions or products referred to in the content.